Pharmacogn. Res., 2027; 19(1):309-318.
https://www.phcogres.com

Original Article

Camellia sinensis Extract Mediated Synthesis of Fe_3O_4 Magnetic Nanoparticles for pH-Responsive Targeted Breast Cancer Therapy

Balaji M B[1], Gulipalli Pallavi[2], Imeiya M U[1], Kedari G S R[1], Vimal S[1,*], Mohamed Saleem T S[3]

[1]Department of Biochemistry, Saveetha Medical College and Hospitals, Saveetha Institute of Medical and Technical Sciences, Saveetha University, Tamil Nadu, INDIA.
[2]Department of General Medicine, Saveetha Medical College and Hospital, Saveetha Institute of Medical and Technical Sciences (SIMATS), Tamil Nadu, INDIA.
[3]Department of Pharmacy, College of Pharmacy, Nursing and Medical Sciences, Riyadh ELM University, Riyadh, SAUDI ARABIA.

ABSTRACT

Objectives: One challenge in treating breast cancer is that there are not enough drug delivery systems that can both target tumors specifically and have their own pharmacological effects. **Materials and Methods:** This study prepared Fe_3O_4 Magnetic Nanoparticles (Cs-MNPs) from a one-pot aqueous reaction using *Camellia sinensis* leaf extract as both reducing agent and surface stabiliser. **Results:** Particles were rod-shaped with dimensions of 30-80 nm verified by FTIR spectroscopy and SEM. Antioxidant testing gave DPPH IC_{50} 85.4±2.3 µg mL^{-1}. BSA thermal denaturation was suppressed by 78.2±1.8% at 50 µg mL^{-1}. The synthesized Nps demonstrated inhibition IC_{50} values of 58.4±1.7 µg mL^{-1} for α-amylase and 47.6±1.8 µg mL^{-1} for α-glucosidase indicating effective enzyme inhibition. Drug release at pH 5.5 reached 72.3% at 24 hr versus 41.6% at pH 7.4. MCF-7 cell viability assay returned IC_{50} 19±0.7 µg mL^{-1} and apoptosis was confirmed by AO/EtBr staining. **Conclusion:** The Cs-MNP system is worth exploring as a green theranostic material.

Keywords: Apoptosis, Breast Cancer, *Camellia sinensis*, DPPH Scavenging, Enzyme Inhibition, Fe_3O_4, Green Synthesis, pH-Responsive Drug Release.

Correspondence:
Dr. Vimal S
Department of Biochemistry, Saveetha Medical College and Hospitals, Saveetha Institute of Medical and Technical Sciences, Saveetha University, Tamil Nadu, INDIA.
Email: vimals.smc@saveetha.com

Received: 27-04-2026;
Revised: 02-06-2026;
Accepted: 15-07-2026.

INTRODUCTION

Breast cancer is the most commonly diagnosed cancer among women worldwide (2.3 million cases annually) and standard treatments including surgery, radiotherapy, chemotherapy along with endocrine therapy improve survival but challenges such as resistance and recurrence persist (Sung *et al.*, 2021; Ibrahim *et al.*, 2024). Metastatic disease still lacks curative options despite these advances (Chaudhari *et al.*, 2024). Drug resistance, molecular heterogeneity within tumour subtypes and dose-limiting toxicity from systemic cytotoxics are the three problems that persistently reduce long-term control. Nanoparticle-based carriers were developed to address these gaps by accumulating drug payloads inside tumour tissue while reducing exposure of healthy organs (Verma *et al.*, 2025). Iron oxide nanoparticles hold a unique position in nanocarrier systems owing to their superparamagnetic properties high surface-to-volume ratio and established biocompatibility (Bhat *et al.*, 2024; Tamang *et al.*, 2025; Lazaro-Carrillo *et al.*, 2020). Magnetite (Fe_3O_4) is cleared from the body through normal iron metabolism without accumulating to toxic levels (Ali *et al.*, 2016). Chemical production routes like coprecipitation and thermal decomposition work but require toxic precursors with high energy input (Iravani *et al.*, 2011). Plant-extract synthesis avoids these costs entirely. Polyphenols within the extract reduce metal salts and cap the particle surface simultaneously, so the finished material carries its own pharmacological toolkit (Shabbir *et al.*, 2023; Abdelrahman *et al.*, 2026). *Camellia sinensis* is a well-characterized polyphenol rich plant dominated by epigallocatechin gallate, epicatechin gallic acid and theaflavin with activities including radical scavenging inflammatory pathway inhibition digestive enzyme suppression and reduced cancer cell proliferation (Capasso *et al.*, 2025; Ajaz *et al.*, 2025). During nanoparticle synthesis they donate electrons to reduce dissolved iron ions into the Fe_3O_4 lattice and then adsorb onto the crystal face, retaining their activity in the finished product (Al Awawdeh *et al.*, 2026). Most published green-synthesis studies test one or two biological endpoints per study. A comprehensive dataset covering antioxidant, anti-inflammatory, antidiabetic, pH-triggered release and cytotoxic properties within a single

OPEN ACCESS

Manuscript TECHNOMEDIA

DOI: 10.5530/pres.20270194

Copyright Information :
Copyright Author (s) 2027 Distributed under Creative Commons CC-BY 4.0

Publishing Partner : Manuscript Technomedia. [www.mstechnomedia.com]

green-tea formulation study has not been reported (Abbas *et al.*, 2026; Al-Harbi *et al.*, 2022). Solid tumour extracellular pH sits between 5.5 and 6.8 because glycolytic activity outpaces vascular lactate clearance (Sengupta *et al.*, 2025; Lameli *et al.*, 2026). A carrier that releases drug preferentially at acidic pH reaches the tumour without any external trigger. This study reports phytofabrication of Fe_3O_4 MNPs via *Camellia sinensis* leaf extract and provides a full biological profile: DPPH scavenging, BSA denaturation inhibition, α-amylase inhibition, α-glucosidase inhibition, pH-dependent release kinetics and MTT cytotoxicity assay was performed on MCF-7 cells followed by AO/EtBr staining to classify the mode of cell death.

MATERIALS AND METHODS

Nps Preparation

The leaves of *C. sinensis* were washed and dried in the air after drying it is boiled in deionised water (10 g per 100 mL) at 80°C for 20 min. The filtered extract was stored at 4°C until use. Iron salt solution was made from 0.1 M $FeCl_3 \cdot 6H_2O$ and 0.05 M $FeSO_4 \cdot 7H_2O$ at a 2:1 molar ratio and heated to 80°C. Plant extract (25 mL) was added dropwise under stirring. Addition of 1 M NaOH raised pH to 10 and a black precipitate formed within minutes. The mixture was held at 80°C for 30 min to complete nucleation is shown in Figure 1. Particles were collected by magnetic decantation, washed with deionised water and ethanol, then dried overnight at 60°C (Falahatpisheh *et al.*, 2025).

Physicochemical Characterisation

Infrared Spectroscopic Analysis (FTIR)

Spectroscopic measurements were carried out using a Nicolet 5700 FTIR instrument (Thermo Scientific, USA). Cs-MNPs were co-ground with KBr and pressed into translucent pellets. Spectra were collected from 500 to 4000 cm^{-1} 20 (Rafieian *et al.*, 2017).

SEM Imaging

A JEOL JSM-5600LV instrument was used. Powder was mounted on polycarbonate stubs and sputter-coated with gold under CO_2 critical-point drying before imaging at 20 kV (Raguldarun *et al.*, 2024).

Cell Culture and Maintenance

The MCF-7 cell line was procured from the National Centre for Cell Sciences (NCCS), Pune, India. Growth medium was DMEM with 10% heat-inactivated FBS, 2 mM L-glutamine, 1.5 g L^{-1} $NaHCO_3$, 0.1 mM non-essential amino acids and 10 mM HEPES. Penicillin (100 IU mL^{-1}) and streptomycin (100 µg mL^{-1}) were included in all flasks. Cells were maintained at 37°C in a humidified atmosphere of 5% CO_2 (Javed *et al.*, 2020).

pH-Dependent Drug Release

Cs-MNPs (20-100 mg) were dispersed in 10 mL PBS at pH 7.4 and pH 5.5 with chitinase (1.5 U mL^{-1}) and shaken at 100 rpm at 37°C. At 1, 2, 4, 8, 12 and 24 hr a 1 mL aliquot was withdrawn and centrifuged at 10 000 rpm for 5 min. Supernatant absorbance at 425 nm was compared against a *Camellia sinensis* extract calibration curve of 0-20 µg mL^{-1}. Withdrawn volume was replaced with fresh buffer to maintain sink conditions:

$$\text{Cumulative release (\%)} = (\text{released at time t / total loaded}) \times 100$$

Data were fitted to zero-order, first-order, Higuchi and Korsmeyer-Peppas models (Roemhild *et al.*, 2026; Anwar *et al.*, 2026).

MTT Cell Viability Assay

Cells were seeded at 1×10^4 per well in 96-well plates and grown to approximately 80% confluency. Cs-MNPs at 0-100 µg mL^{-1} were applied and plates incubated for 48 hr. MTT reagent [3-(4,5-dimethylthiazol-2-yl)-2,5-diphenyltetrazolium bromide] at 0.5 mg mL^{-1} was added (100 µL per well) and incubated 4 hr at 37°C. After aspirating medium, formazan was dissolved in 50 µL DMSO and absorbance read at 620 nm on a Thermo Multiskan EX reader.

$$Cell\ viability(\%) = \left(\frac{OD\ of\ treated\ sample}{OD\ of\ control}\right) x\ 100$$

IC_{50} was obtained by non-linear regression from triplicate experiments (Abbas *et al.*, 2025).

Bright-Field Morphology

MCF-7 cells at 1×10^5 per coverslip were seeded in 6-well plates and allowed overnight adhesion. Medium was swapped for IC_{50}-containing DMEM and cells incubated a further 24 hr. Coverslips were fixed in ethanol:acetic acid (3:1) and examined at ×10 on a Nikon inverted microscope.

AO/EtBr Fluorescence Staining

Cells were washed in PBS (pH 7.2) and stained 2 min with a 1:1 acridine orange/ethidium bromide mixture at 100 µg mL^{-1} each. Images were taken on a Nikon Eclipse fluorescence microscope at ×10. Acridine orange enters intact cells and labels double-stranded DNA green. Ethidium bromide penetrates cells with damaged membranes and stains nucleic acids orange-red (Rajeshkumar *et al.*, 2022).

DPPH Radical Scavenging

Cs-MNPs were tested at 20, 40, 60, 80 and 100 µg mL^{-1} against 0.1 mM 2,2-diphenyl-1-picrylhydrazyl in methanol. Equal volumes (100 µL each) were mixed in foil-covered 96-well plates and left for 30 min at room temperature. Absorbance was read at 517 nm

with ascorbic acid as the reference compound (Al-Zabin *et al.*, 2024; Sharma *et al.*, 2026).

$$\% \, Inhibition - \frac{Absorbance\ of\ Control - Absorbance\ of\ the\ sample}{Absorbance\ of\ Control} \, x\ 100$$

BSA Denaturation Inhibition

BSA solution (0.45 mL of 1% w/v) was mixed with 0.05 mL Cs-MNP suspension at 20-100 µg mL^{-1}. pH was adjusted to 6.3 with 1 N HCl and the mixture held at room temperature 20 min before heating to 55°C for 30 min. Turbidity at 660 nm indicated protein aggregation. DMSO was the blank and diclofenac sodium was the reference drug. One-way ANOVA with Tukey post-hoc test was used (Sharma *et al.*, 2024).

$$\% \, Inhibition = \frac{Absorbance\ of\ Control - Absorbance\ of\ the\ sample}{Absorbance\ of\ Control} \, x\ 100$$

Enzyme Inhibition Assays

For α-amylase: 1% soluble starch in 20 mM phosphate buffer (pH 6.9) was incubated with α-amylase (1 U mL^{-1}) and Cs-MNPs at 20-100 µg mL^{-1} for 30 min at 37°C. DNS reagent was added and tubes boiled 5 min then read at 540 nm. For α-glucosidase: p-nitrophenyl α-D-glucopyranoside in 20 mM phosphate buffer (pH 6.8) was substrate. Enzyme (1 U mL^{-1}) and Cs-MNPs were incubated for 30 min at 37°C then reaction stopped with 0.1 M Na_2CO_3. Released p-nitrophenol was read at 405 nm. Acarbose was the positive control. IC_{50} values obtained by non-linear regression with one-way ANOVA (Lakshya *et al.*, 2026; Bharathidasan *et al.*, 2023).

Statistical Analysis

Statistical analysis was performed using GraphPad Prism 14.2 and OriginPro 2025b. Data are presented as mean ± Standard Deviation (SD) of at least three independent experiments.

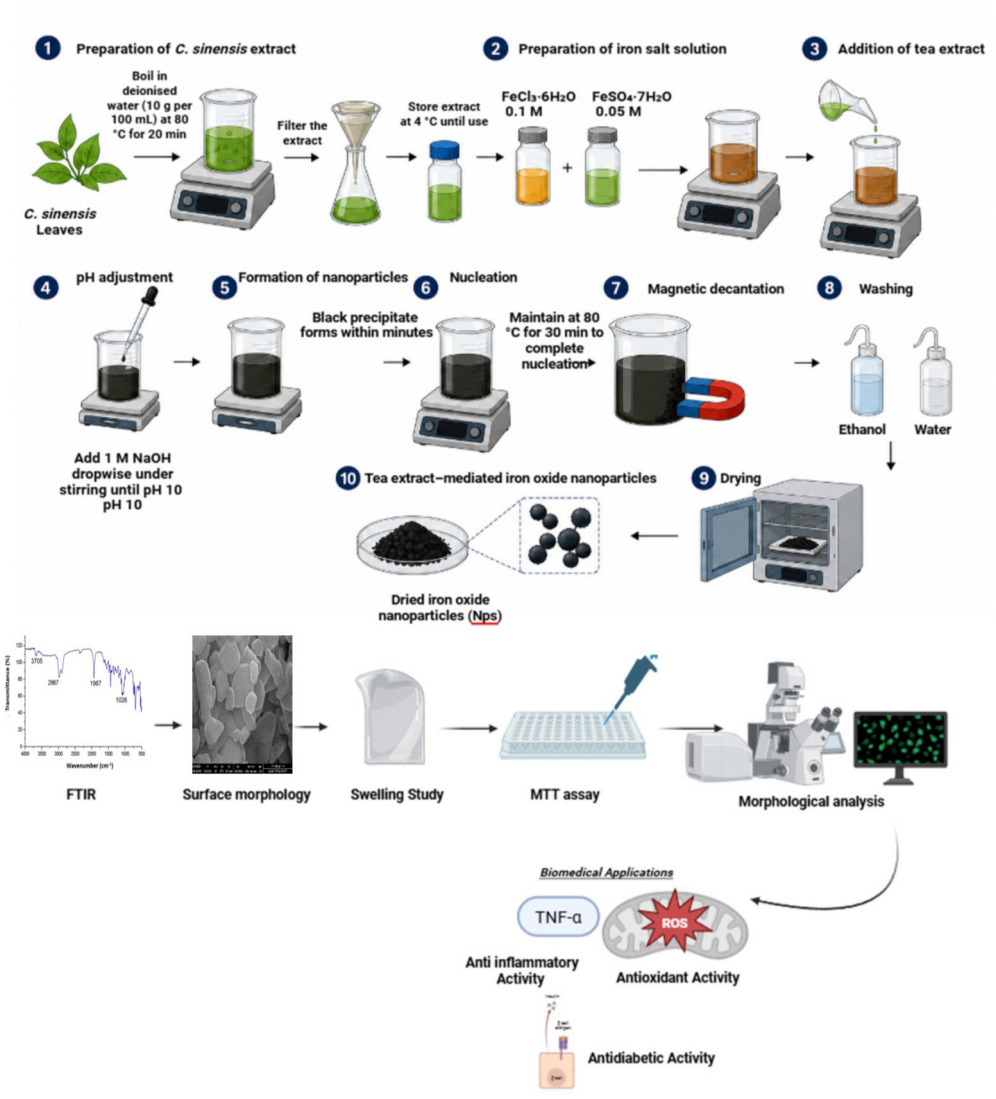


Figure 1: Green synthesis of iron oxide nanoparticles using *Camellia sinensis* leaf extract.

Differences among multiple groups were evaluated using One-Way Analysis of Variance (ANOVA) followed by Tukey's *post hoc* test. A p-value <0.05 was considered statistically significant.

RESULTS AND COMPARATIVE ANALYSIS

Infrared Spectroscopic Analysis (FTIR)

FTIR data pointed to polyphenol retention on the nanoparticle surface in Figure 2A. A broad O-H stretch near 3705 cm^{-1} arose from catechin hydroxyl groups with high intensity, indicating substantial surface polyphenol loading. A C-H stretch at around 2987 cm^{-1} was consistent with methyl and methylene groups of secondary metabolites. The peak at 1026 cm^{-1} belongs to C-O stretching of ether and alcohol units in polyphenol backbones (Calero *et al.*, 2015). The 1700-1750 cm^{-1} region showed no carbonyl absorption, indicating catechins were not oxidised during synthesis so phenolic O-H groups stayed intact. Signals below 600 cm^{-1} correspond to Fe-O lattice vibrations, verifying a crystalline Fe_3O_4 core formed beneath the polyphenolic layer.

Surface Morphology

Micrographs showed rod-shaped particles rather than the spheres typical of chemical magnetite (Figure 2B). Width and length measurements from the images placed particles within 30-80 nm. Particle clustering was visible throughout the sample and was attributed to magnetic dipole-dipole forces between individual nanorods reinforced by polyphenol bridges between adjacent surfaces (Peer *et al.*, 2007). The rod habit likely arises from anisotropic crystal growth at the high alkaline pH of the synthesis. Surface texture appeared rough with irregular topography consistent with simultaneous nucleation at many chemically distinct sites in the polyphenol mixture. The 30-80 nm size range is too large for rapid renal clearance yet small enough (Sengupta *et al.*, 2025).

pH-Triggered Drug Release

Both pH conditions produced a biphasic release curve with rapid early release levelling to a plateau after approximately 12 hr shown in Table 1 and Figure 2C. At pH 5.5 cumulative release reached 72.3±2.8% by 24 hr versus only 41.6±2.1% at pH 7.4

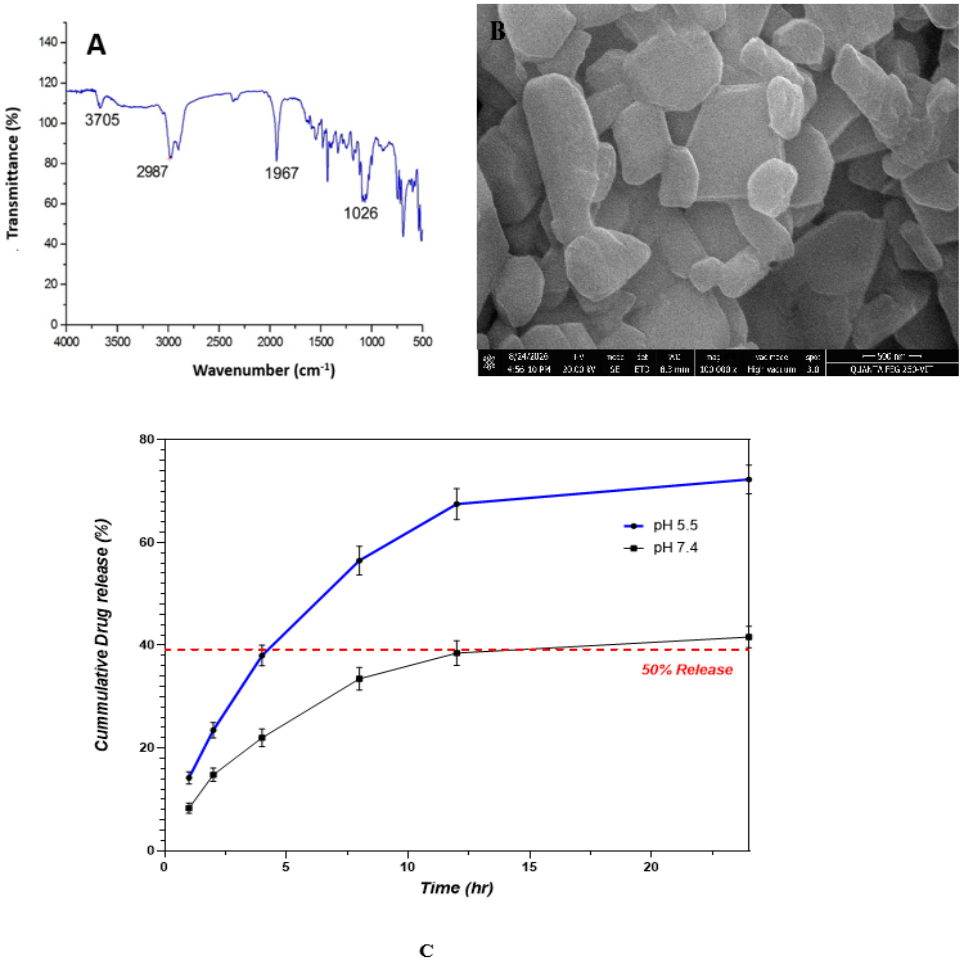


Figure 2: Physicochemical characterization of Cs-MNPs. (A) FTIR spectrum showing characteristic polyphenol and Fe-O functional groups. (B) SEM micrograph revealing rod-shaped morphology and nanoparticle aggregation (c) Cumulative drug release (%) of Cs-MNPs at pH 5.5 and pH 7.4 over 24 hr at 20, 40, 60, 80, and 100 µg/mL (n=3, mean ± SD).

(p<0.05), an enhancement ratio of 1.74. Acidification protonates surface phenolic hydroxyls and weakens the electrostatic and H-bonding interactions anchoring the polyphenol cargo to the Fe_3O_4 surface, so release accelerates. Tumour extracellular *p*H at 5.5-6.8 arises from glycolysis-derived lactate accumulation when vascular clearance is insufficient (Sengupta *et al.*, 2025; Roemhild *et al.*, 2026). The Korsmeyer-Peppas model fitted the pH 5.5 profile with R^2=0.99. The diffusion exponent n=0.52 lies between pure Fickian diffusion and Case II polymer relaxation release is anomalous non-Fickian. Molecular diffusion through the polyphenol coat and matrix.

Biomedical Applications

Antioxidant Activity

DPPH scavenging rose from 22.4±1.2% at 20 µg mL^{-1} to 91.2±1.4% at 100 µg mL^{-1} (Table 2 and Figure 3A). IC_{50} was 85.4±2.3 µg mL^{-1} versus 42.6±1.1 µg mL^{-1} for ascorbic acid under the same conditions. The phenolic hydroxyls on surface-bound catechins donate hydrogen to the unpaired nitrogen radical of DPPH to produce a stable colourless form. Published IC_{50} values for plant-derived iron oxide particles generally fall between 75 and 120 µg mL^{-1}. So, the result here falls within a normal range. The dual capacity of the polyphenol shell to scavenge radicals extracellularly and of the Fe_3O_4 core to generate intracellular radicals via Fenton chemistry has been recognised in iron-based nanomedicine (Abbas *et al.*, 2026).

Anti-Inflammatory Properties

Cs-MNPs suppressed BSA thermal denaturation in a dose-dependent pattern in Figure 3B and Table 3. At 20 µg mL^{-1} inhibition was 34.5±1.3% and at 100 µg mL^{-1} it rose to 78.2±1.8% compared with 84.6±2.0% for diclofenac sodium at the same dose. This represents 92% of reference drug activity for a material without a dedicated anti-inflammatory pharmacophore and IC_{50}

Table 1: Summary statistics showing higher drug release at pH 5.5 than pH 7.4 (enhancement ratio 1.74) with Korsmeyer-Peppas model fitting (R^2=0.99) and anomalous diffusion behavior (n=0.52).

Parameter	Value
Max release pH 5.5 (%)	72.30
Max release pH 7.4 (%)	41.60
Enhancement ratio (5.5/7.4)	1.74
Korsmeyer-Peppas R^2	0.99
Diffusion exponent n	0.52

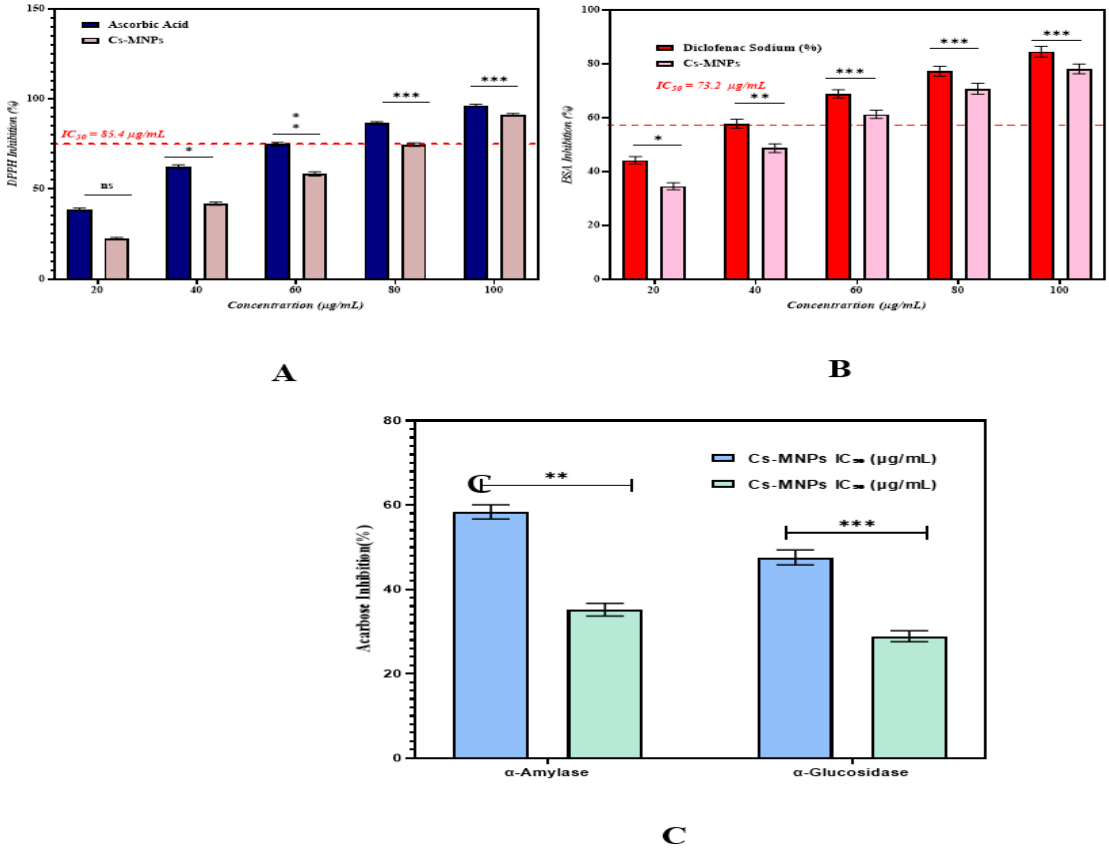


Figure 3: Biological activities of Cs-MNPs. (A) DPPH radical scavenging activity (%) of Cs-MNPs compared with ascorbic acid at concentrations of 20, 40, 60, 80, and 100 µg/mL. (B) Anti-inflammatory activity determined by BSA denaturation inhibition (%) of Cs-MNPs compared with diclofenac sodium at concentrations of 20, 40, 60, 80, and 100 µg/mL. (C) Antidiabetic activity showing α-amylase and α-glucosidase inhibition by Cs-MNPs compared with acarbose. Data are presented as mean ± SD (n=3).

is 73.2±2.3 µg. EGCG on the particle surface suppresses NF-κB and AP-1 signalling pathways while reducing COX-2 expression and IL-6 and TNF-α secretion (De Mezer *et al*., 2025). Chronic tumour-associated inflammation supports drug resistance and metastatic spread, so this inhibitory activity has potential to complement the cytotoxic component of the formulation.

Evaluation of Antidiabetic Assay

The pathogenesis of type 2 diabetes via chronic hyperinsulinaemia and this axis directly drives breast tumour proliferation (Lakshya *et al*., 2026; Bharathidasan *et al*., 2023). Reducing postprandial glucose and insulin spikes through carbohydrate-enzyme inhibition may lower that growth stimulus at least partially. Cs-MNPs inhibited both enzymes across the full concentration range tested shown in Figure 3 and Table 4. α-Amylase inhibition reached 68.5±2.1% at 100 µg mL^{-1} with IC_{50} 58.4±1.7 µg mL^{-1}. α-Glucosidase was inhibited more strongly at 74.3±1.9% with IC_{50} 47.6±1.8 µg mL^{-1} versus 28.9±1.3 µg mL^{-1} for acarbose. EGCG and gallic acid at the surface fit enzyme active sites via hydrogen bonding and hydrophobic contacts to block substrate entry (Capasso *et al*., 2025; Abbas *et al*., 2026).

MCF-7 Cytotoxicity

Cell viability decreased with increasing Cs-MNP concentration across 48 hr is shown in *and* Figure 4A. At 20 µg mL^{-1} viability was 82.4% and at 100 µg mL^{-1} it fell to 8.3±0.6%. IC_{50} was 19 ± 0.7 µg mL^{-1} and one-way ANOVA with Tukey test confirmed each concentration point differed from untreated control ($p<0.05$) with 95% confidence intervals shown in Tables. The kill mechanism is likely multifactorial. Ferrous ions from the core react with intracellular H_2O_2 via Fenton chemistry to generate hydroxyl radicals that damage DNA and membrane lipids. Mitochondrial depolarization releases cytochrome c and triggers the caspase cascade. Iron overload disrupts cellular ion homeostasis. EGCG on the surface independently blocks NF-κB, PI3K/Akt and HER2 receptor pathways (Capasso *et al*., 2025; Alagarsamy *et al*., 2025). The IC_{50} of 19 µg mL^{-1} is lower than most published values for plant-mediated iron oxide nanoparticles against MCF-7 cells (Al-Harbi *et al*., 2022).

Cell Morphology

Untreated MCF-7 cells were flat, polygonally spread and firmly attached to the substrate surface. Cells treated at IC_{50} showed a strikingly different picture: rounded shrunken bodies with dense dark cytoplasm, surface membrane blebbing and widespread detachment from the substrate (Figures 4B and 4C). Cell rounding and cytoplasmic condensation are hallmarks of ordered cytoskeletal disassembly during apoptosis. Membrane blebs form when caspases cleave the actin cortex below the plasma membrane. Detachment results from proteolytic degradation of focal adhesion proteins (Alagarsamy *et al*., 2025; Chandramohan *et al*., 2024). Necrotic cells do the opposite by swelling and bursting, so the shrinkage and condensation pattern observed here rules out necrotic death.

Apoptosis Verification by AO/EtBr

Fluorescence staining put the morphological data on a molecular basis (Figures 4D and 4E). Control cells produced uniform green emission confirming intact membranes and viable nuclei. Treated cells shifted to yellow-orange emission because ethidium bromide displaced acridine orange from nucleic acid binding sites after membrane integrity was lost. Many stained nuclei showed pyknosis and karyorrhexis, which are features definitional for apoptosis and absent in necrotic cells whose nuclei swell and dissolve (Rajeshkumar *et al*., 2022; Alagarsamy *et al*., 2025). Taken together with the MTT dose-response data, the staining pattern confirms that Cs-MNPs induce programmed rather than necrotic death in MCF-7 cells.

DISCUSSION

The complete dataset shows Fe_3O_4 nanoparticles made from *Camellia sinensis* extract carry a pharmacologically active polyphenol coat. FTIR data showed catechins stayed in their reduced phenolic form throughout the reaction. Retention of O-H groups explains why the finished particles scavenge DPPH, suppress protein denaturation and inhibit digestive enzymes. Gallic acid and EGCG both carry multiple aromatic hydroxyl groups that fit enzyme active sites via H-bonding and hydrophobic contact (Capasso *et al*., 2025; Abbas *et al*., 2026). The chemistry of the extract is the key bridge between synthesis conditions and biological output. Reactive oxygen species

Table 2: DPPH radical scavenging activity of Cs-MNPs alongside ascorbic acid as positive control.

Concentration (µg/mL)	MNPs		Acarbose (AA)	
	Mean (%)	SD (±)	Mean (%)	SD (±)
20	22.40	0.63	38.60	0.79
40	41.80	0.90	62.40	0.95
60	58.30	1.11	74.80	1.06
80	74.60	1.01	86.50	0.85
100	91.20	0.74	96.30	0.69

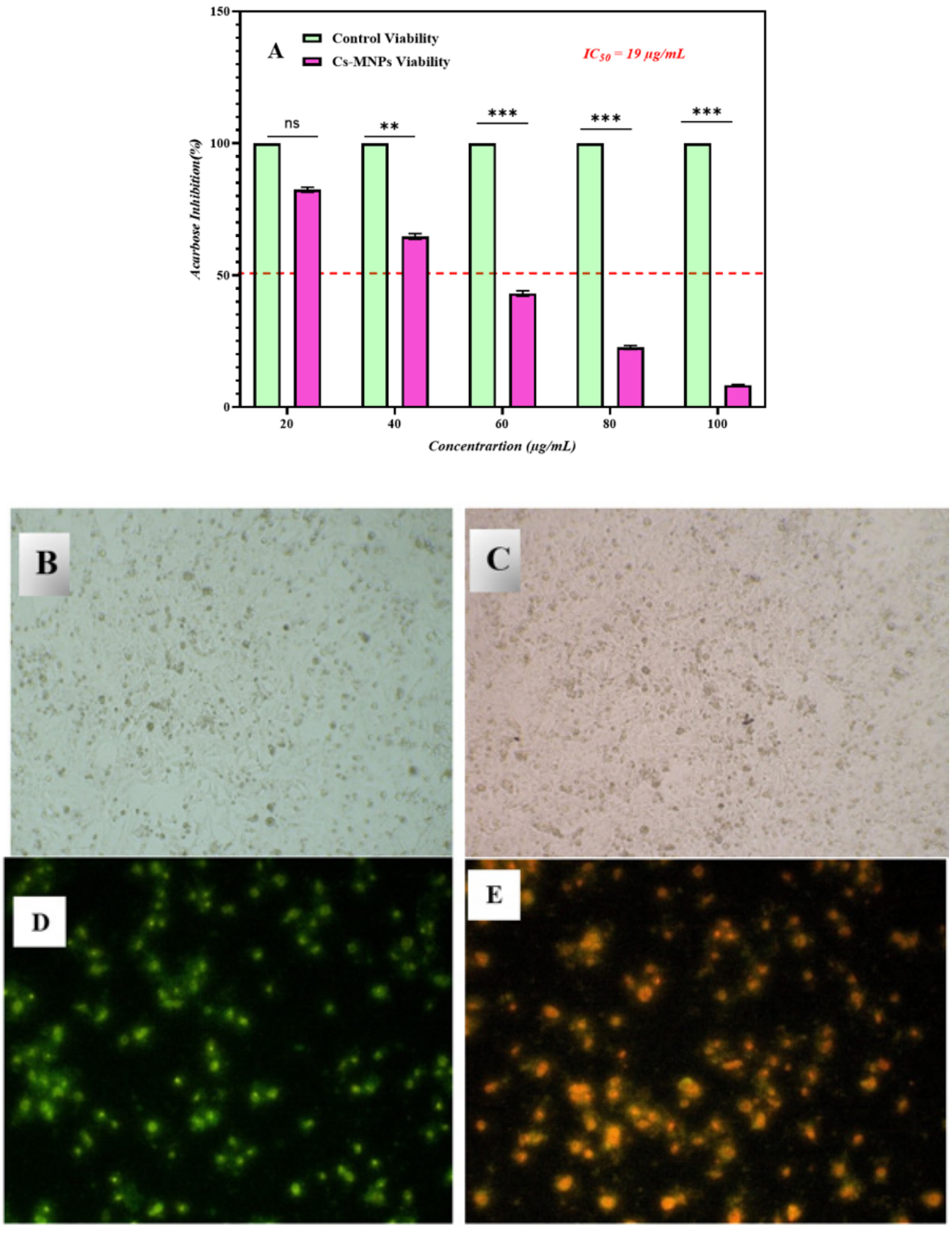


Figure 4: Anticancer activity and apoptosis induction by Cs-MNPs in MCF-7 cells. (A) MTT assay showing concentration-dependent reduction in cell viability after 48 hr treatment. (B-C) Morphological changes in treated cells, including cell shrinkage, membrane blebbing, and nuclear condensation. (D) AO/EtBr-stained untreated cells showing viable green fluorescence. (E) AO/EtBr-stained treated cells showing orange-red fluorescence indicative of apoptosis.

Table 3: BSA denaturation inhibition (%) by Cs-MNPs compared with diclofenac sodium.

Concentration (µg/mL)	Cs-MNPs		Diclofenac Sodium	
	% Inhibition	SD (±)	% Inhibition	SD (±)
20	34.5	1.3	44.2	1.4
40	48.7	1.6	57.8	1.7
60	61.3	1.5	68.9	1.5
80	70.8	2.0	77.3	1.9
100	78.2	1.8	84.6	2.0

Table 4: IC_{50} values (microgram/mL) for enzyme inhibition by Cs-MNPs versus acarbose.

Assay	Cs-MNPs IC_{50}		Acarbose IC_{50}		Ratio MNP/Acarbose
	(µg/mL)	SD (±)	(µg/mL)	SD (±)	
Alpha-amylase inhibition	58.4	1.7	35.2	1.5	1.66
Alpha-glucosidase inhibition	47.6	1.8	28.9	1.3	1.65

have a context-dependent relationship with cancer cells. At moderate levels they support oncogenic mutation at the start of carcinogenesis and at high levels they push established cancer cells into programmed death (Al-Zabin *et al.*, 2024; Sharma *et al.*, 2026). Iron oxide particles exploit this relationship from both ends. The polyphenol shell scavenges extracellular radicals near normal tissue. The Fe_3O_4 core, after endocytosis, reacts with intracellular H_2O_2 to spike reactive oxygen species above the cancer cell survival threshold. This site-selective duality is a recognised property of iron-based nanomedicine (Abbas *et al.*, 2026). Tumour-associated chronic inflammation contributes to drug resistance, metastatic spread and the wasting syndrome seen in advanced disease. EGCG at the nanoparticle surface targets NF-κB and AP-1 activation and reduces COX-2 expression together with IL-6 and TNF-α output (Ajaz *et al.*, 2025). Suppressing those signals in the tumour microenvironment lowers inflammatory barriers that normally protect cancer cells from cytotoxic treatment. The diabetes-to-cancer connection through insulin signalling pathways is epidemiologically well-supported (Lakshya *et al.*, 2026; Bharathidasan *et al.*, 2023). α-Glucosidase and α-amylase inhibition slows postprandial glucose absorption and blunts insulin pulses. That in turn can reduce PI3K/Akt/mTOR pathway activity driven by chronic hyperinsulinaemia in mammary tissue. The enzyme IC_{50} data reported here are an *in vitro* starting point and animal metabolic data are needed to validate this mechanism. The 1.74-fold among pH shows the polyphenolic coat responds to tumour microenvironmental acidity without any external trigger. The Korsmeyer-Peppas exponent of 0.52 shows release is not simple Fickian diffusion nor full chain relaxation but a blend of both. This profile enables the maintenance of sustained drug conc the target site in contrast to the transient bolus spikes typically observed with purely diffusion-controlled systems (Roemhild *et al.*, 2026; Anwar *et al.*, 2026). IC_{50} at 48 hr is competitive with published values for plant-derived iron oxide formulations on the same cell line. Apoptotic rather than necrotic death is immunologically preferred because apoptosis does not release pro-inflammatory damage signals that can paradoxically support survival of residual cancer cells (Alagarsamy *et al.*, 2025; Chandramohan *et al.*, 2024). The Cs-MNP system integrates a scalable green synthesis route, a multifunctional polyphenol coat providing antioxidant, anti-inflammatory and antidiabetic activity, a tumour-pH-gated release mechanism and a potent selective cytotoxic effect in one material made from water and plant extract (Dey *et al.*, 2024; Khan *et al.*, 2013).

CONCLUSION

Fe_3O_4 nanoparticles were produced from *Camellia sinensis* extract in a single aqueous step with no synthetic reductants. FTIR confirmed polyphenol retention via intact O-H groups and SEM placed particle size at 30-80 nm with a rod-like shape Five biological endpoints were evaluated. First, the DPPH IC_{50} was 85.4±2.3 µg mL^{-1}. Additionally, BSA denaturation inhibition reached 78.2±1.8% at 50 µg mL^{-1}. Furthermore, the α-glucosidase IC_{50} was 47.6±1.8 µg mL^{-1} and the α-amylase IC_{50} was 58.4±1.7 µg mL^{-1}. In terms of release studies, at pH 5.5 the release was 72.3%, compared to 41.6% at pH 7.4 over 24 hr. Finally, the MCF-7 IC_{50} was 19±0.7 µg mL^{-1} and apoptotic cell death was confirmed by AO/EtBr staining. No single endpoint stands alone here the polyphenol coat and magnetite core each add therapeutic dimensions the other does not provide. *In vivo* efficacy, toxicity studies apoptotic pathway mapping, loading optimisation and reproducible scale-up are the minimum steps needed before clinical translation.

ACKNOWLEDGEMENT

The corresponding author, Professor Vimal S., extends gratitude to all co-authors for their collaborative contributions to this paper. This work was supported by the Department of Biochemistry, Saveetha Medical College and Hospital, Saveetha Institute of Medical and Technical Sciences (SIMATS), Thandalam, Chennai-600105, Tamil Nadu, India.

ABBREVIATIONS

AO/EtBr: Acridine Orange/Ethidium Bromide; **AP-1:** Activator protein 1; **BSA:** Bovine Serum Albumin; **COX-2:** Cyclooxygenase-2; **Cs-MNPs:** *Camellia sinensis* Magnetic Nanoparticles; **DMEM:** Dulbecco's Modified Eagle Medium; **DMSO:** Dimethyl Sulfoxide; **DNS:** 3,5-Dinitrosalicylic acid; **DPPH:** 2,2-diphenyl-1-picrylhydrazyl; **EGCG:** Epigallocatechin gallate; **FBS:** Fetal Bovine Serum; **FTIR:** Fourier Transform Infrared; **HER2:** Human Epidermal Growth Factor Receptor 2; **IL-6:** Interleukin 6; **MCF-7:** Michigan Cancer Foundation-7; **mTOR:** Mammalian target of rapamycin; **MTT:** 3-(4,5-dimethylthiazol-2-yl)-2,5-diphenyltetrazolium bromide; **NF-κB:** Nuclear factor kappa B; **PBS:** Phosphate Buffered Saline; **PI3K/Akt:** Phosphoinositide 3-kinase/Protein Kinase B; **SEM:** Scanning Electron Microscope; **TNF-α:** Tumor necrosis factor alpha.

CONFLICT OF INTEREST

The authors declare that there is no conflict of interest.

SUMMARY

Camellia sinensis leaf extract was successfully utilized for the green synthesis of Fe_3O_4 Magnetic Nanoparticles (Cs-MNPs) through a simple aqueous method.

FTIR and SEM analyses confirmed polyphenol-capped Fe_3O_4 nanoparticles with rod-shaped morphology and particle sizes ranging from 30-80 nm.

Cs-MNPs exhibited significant antioxidant activity (DPPH IC_{50}=85.4±2.3 μg mL^{-1}), anti-inflammatory activity (78.2±1.8% inhibition of BSA denaturation), and antidiabetic potential through α-amylase and α-glucosidase inhibition.

The nanoparticles demonstrated pH-responsive release behavior, with enhanced release at acidic pH (72.3% at pH 5.5) compared to physiological pH (41.6% at pH 7.4).

Cytotoxicity studies against MCF-7 breast cancer cells showed potent anticancer activity (IC_{50}=19±0.7 μg mL^{-1}), and AO/EtBr staining confirmed apoptosis as the primary mode of cell death.

These findings suggest that Cs-MNPs are promising multifunctional nanomaterials for targeted breast cancer therapy and warrant further *in vivo* investigation.

REFERENCES

Abbas, J., Jabeen, A., Ajmal, A., et al. (2026). Biogenic synthesis of antimicrobial, anti-inflammatory, antioxidant and biocompatible iron oxide nanoparticles from Arthrospira sp. extract. Discover Nano, 21(1), 40.

Abbas, R., Muzammil, S., Khurshid, M., & Hayat, S. (2025). Antibiofilm, antioxidant and photocatalytic potential of iron oxide nanoparticles biofabricated from plant extract. RSC Advances, 15(54), 46009-46023.

Abdelrahman, E. A., Alhamzani, A. G., Abou-Krisha, M. M., El-Sayyad, G. S., & Abd El-Aziz, S. M. (2026). Assessing extracts of Laurencia obtusa algae for green fabrication of magnetic nanoparticles. Food Chemistry, 508(Pt A), 148319.

Ajaz, F., Haddad, J., Huda, B., et al. (2025). Epigallocatechin gallate as a molecular therapeutic in heart failure and cardio-oncology. International Journal of Molecular Sciences, 26(21), 10798.

Al-Harbi, *L. N.,* Al-Shammari, G. M., Subash-Babu, P., et al. (2022). Phytochemicals-loaded iron oxide nanoparticles induce cytotoxicity and apoptosis in MCF-7 breast cancer cells. N*anomate*rials, 12(19), 3393.

Al-Zabin, A., Abu Thiab, T., Zihlif, M., et al. (2024). Anti-angiogenic and cytotoxic evaluation of green-synthesized FeZnO nanoparticles against MCF-7 cells. Biomedical Reports, 20(3), *36.*

Alagarsamy, K., Chaiyasut, C., Kesika, P., & Sivamaruthi, B. S. (2025). Impact of green tea (Camellia sinensis L.) on oral health. Current Pharmaceutical Design.

Ali, *A.,* Zafar, H., Zia, M., et al. (2016). Synthesis, characterization, applications and challenges of iron oxide nanoparticles. Nanotechnology, Science and Applications, 9, 49-67.

Al Awawdeh, S., Shafie, N. H., Ishak, A. H., et al. (2026). In vitro release kinetics and in vivo plasma exposure of g*reen tea* polyphenols from iron oxide chitosan nanoparticles. Scientific Reports, 16(1), 5438.

Anwar, T., Qureshi, H., Imran, M., et al. (2026). Arsenic uptake and detoxification modulation in maize by plant-based iron oxide nanoparticles. Biodegradation, 37(2).

Bharathidasan, P., Sundar, S., Shanmugam, R. K., *et al.* (2023). Antioxidant, anti-inflammatory and antidiabetic activity of oolong-tea-mediated strontium nanoparticles. Journal of Population Therapeutics and Clinical Ph*armacol*ogy, 30(8), 511-516.

Bhat, S. A., Kumar, V., Dhanjal, D. S., et al. (2024). Biogenic nanoparticles: Pioneering a new era in breast cancer therapeutics. Discover Nano, 19*(1),* 121.

Calero, M., Chiappi, M., Lazaro-Carrillo, A., et al. (2015). Characterisation of magnetic nanoparticle interactions with breast cancer cells. Journal of Nanobiotechnology, 13, 16.

Capasso, L., *De M*asi, L., *Sirignano*, C., et al. *(2025).* Epigallocatechin gallate (EGCG): Pharmacological properties, biological activities and therapeutic potential. Molecules, 30(3), 654.

Chandramohan, S., Francis, *A. P.,* Pajaniradje, S., et al. (2024). Green and chemically synthesised zinc oxide nanoparticles: Anti-proliferative activity against breast cancer cells. Particulate Science and Technology, 42(7), 1155-1177.

Chaudhari, R., Patel, *V., &* Kumar, A. (2024). Cutting-edge approaches for targeted drug delivery in breast cancer: Beyond conventional therapies. Nanoscale Advances, 6(9), 2270-2286.

de Mezer, M., Markowska, A., Pietras, J., et al. (2025). The role of Epigallocatechin Gallate (EGCG) in uterine myomas. Biomedicine and Pharmacotherapy, 189, 118345.

Dey, S., et al. (2024). Mycosynthesis of zinc oxide nanoparticles from Lentinula e*dodes:* Antidiabetic, antimicrobial and antioxidant efficacy. Asian Journal of Chemistry, 36(9).

Falahatpisheh, S., Naghib, S. M., Naimi-Jamal, M. R., Jafari, K. M., & Sartipzadeh, O. (2025). Chitosan/agarose-encapsulated oleic acid-coated magnetite nanoparticles as a drug delivery scaffold. International Journal of Biological Macromolecules, 311(Pt 1), 143409.

Ibrahim, M., Fathalla, Z., Al Fatease, A., Alamri, A. H., & Abdelkader, H. (2024). Breast cancer epidemiology, diagnostic barriers and contemporary trends in breast nanotheranostics. Expert Opinion on D*rug Delivery, 21*(12), 1735-1754.

Iravani, S. (2011). Green synthesis of metal nanoparticles using plants. Green Chemistry, 13(10), 2638-2650.

Javed, R., Zia, M., Naz, *S., et al.* (*2020). Role of cap*ping agents in nanoparticle applications in biomedicine and environmental remediation. Journal of Nanobiotechnology, 18(1), 1-15.

Khan, N., & Mukhtar, H. *(*2013). Tea and health: Studies in humans. Current Pharmaceutical Design, 19(34), 6141-6147.

Lakshya, Kaur, A., Tyagi, U., et al. (2026). Phytosynthesized silver nanoparticles from waste Kigelia africana flowers. ChemistryOpen, 15(4), e70187.

Lameli, C., David, S., Allard-Vannier, E., et al. (2026). Development of anti-EGFR targeted magnetic nanoparticles for doxorubicin delivery into *triple* negative breast cancer cells. European Journal of Pharmaceutics and Biopharmaceutics, 222, 115009.

Lazaro-Carrillo, A., Calero, M., Aires, A., et al. (2020). Tailored functionalized magnetic nanoparticles *to tar*get breast cancer cells including cancer stem-like cells. Cancers, 12(6), 1397.

Peer, D., Karp, J. M., Hong, S., et al. (2007). Nanocarriers as an emerging platform for cancer therapy. Nature Nanotechnology, 2(12), 751-760.

Rafieian-Kopaei, M., & Movahedi, M. (2017). Breast cancer chemopreventive and chemotherapeutic effects of Camellia sinensis : An updated review. Electronic Physician, 9(2), 3838-3844.

Raguldarun, P., Arthanari, A., & Kumar, R. *(2024). Green s*ynthesis of iron oxide nanoparticles using Azadirachta indica and Zingiber officinale and embryonic toxicology evaluation. International Journal of Applied Engineering and Technology, 6(1), 47-53.

Rajeshkumar, S., Parameswari, R. P., et al. (20*22). Apoptotic* and antioxidant activity of gold nanoparticles from marine brown seaweed: An in vitro study. BioMed Research Internatio*nal,* 2022, 5746761.

Roemhild, K., Li, Y., Barmin, R. A., et al. (2026). Iron oxide nanoparticle effects on macrophage polarisation, tumour growth and microenvironment modulation. Journal of Controlled Release, 392, 114726.

Seng*upta,* S., Bhattacharjee, A., Basu, B., Kar, S., & Moulik, S. (2025). Ultrasound-mediated nanocarrier-based drug delivery in breast cancer therapy. Journal of Ultrasound in Medicine, 45(4), 735-752.

Shabbir, M. A., Naveed, M., Rehman, S. U., et al. (2023). Synthesis of iron oxide nanoparticles from plant extract and assessment of cytotoxic, antioxidant, anti-inflammatory and anti-*diabeti*c properties. ACS Omega, 8(37), 33358-33366.

Sharma, A. D., Chhabra, R., Rani, J., Chauhan, A., Kaur, I., & Kapoor, G. (2024). Nanoemulsions f*rom Calotropis gigantea* essential oil: Synthesis and anti-cancer and anti-inflammatory evaluation. Journal of Biomaterials Science, Polymer Edition, 35(16), 2506-2527.

Sharma, *S.,* Srivastava, S., & Chaudhary, A. (2026). Box-Behnken design for optimisation of Curcuma caesia-mediated copper oxide nanoparticle synthesis. Biochemical and Biophysical Research Communications, 807, 153414.

Tamang, R., *Mehata, A. K.,* Singh, V., *et al*. (2025). Sustainable synthesis of Camellia sinensis -mediated silver nanoparticles and their anti*cancer m*echanisms in breast cancer cells. Biomaterials Advances, 166, 214072.

Verma, R., Kumar, K., Bhatt, S. (2025). Untangling breast cancer: Trailing towards nanoformulations-based drug de*velopmen*t. Recent Patents on Nanotechnology, 19(1), 76-98.

Sung, H., Ferlay, J., Siegel, R. L., *et al*. (2021). Global cancer statistics 2020: GLOBOCAN estimates of incidence and mortality worldwide for 36 cancers in 185 countries. CA: A Cancer Journal for Clinicians, 71(3), 209-249.

Cite this article: Balaji MB, Gulipalli Pallavi, Imeiya MU, Kedari GSR, Vimal S, *et al*. *Camellia sinensis* Extract Mediated Synthesis of Fe_3O_4 Magnetic Nanoparticles for pH-Responsive Targeted Breast Cancer Therapy. Pharmacog Res. 2027;19(1):309-18.